Optimizing the Ratio of Sn4+ and Sn2+ in Cu2ZnSn(S,Se)(4) Precursor Solution via Air Environment for Highly Efficient Solar Cells

Guang-Xing Liang, Zi-Xuan Yu, Zhi-Gao Xie, Yang He, Jin-Hong Lin, Shuo Chen, Zhuang-Hao Zheng, Jing-Ting Luo, Ping Fan, Zheng-Hua Su, et al.

Optimizing the ratio of Sn^{4+} and Sn^{2+} in $Cu_2ZnSn(S,Se)_4$ precursor solution via air environment for highly efficient solar cells

Guang-Xing Liang[1], Zi-Xuan Yu[1], Zhi-Gao Xie[1], Yang He[1], Jin-Hong Lin[1], Shuo Chen[1], Zhuang-Hao Zheng[1], Jing-Ting Luo[1], Ping Fan[1], Zheng-Hua Su[1], Hong-Li Ma[2], Xiang-Hua Zhang[2]*

[1]Shenzhen Key Laboratory of Advanced Thin Films and Applications, Key Laboratory of Optoelectronic Devices and Systems, College of Physics and Optoelectronic Engineering, Shenzhen University, Shenzhen, 518060, P. R. China

[2] Univ Rennes, CNRS, ISCR (Institut des Sciences Chimiques de Rennes) UMR 6226, Rennes, F-35000, France

E-mail: zhsu@szu.edu.cn

Keywords: $Cu_2ZnSn(S,Se)_4$, solar cells, precursor solution, interface recombination, deep level defects

The use of different Sn valence states (such as Sn^{4+} and Sn^{2+}) in the $Cu_2ZnSn(S,Se)_4$ (CZTSSe) precursor solution is especially important for the quality of the subsequent growth of the CZTSSe films. The latest study has found that replacing $SnCl_2{\cdot}2H_2O$ with anhydrous $SnCl_4$ can remarkably improve the performance of CZTSSe solar cells, but it needs to be operated in the glove box. Herein, for the precursor solution, we use $SnCl_4{\cdot}5H_2O$ powder instead of anhydrous $SnCl_4$ in air environment, and the proportion of Sn^{4+} and Sn^{2+} precursor solutions is further systematically studied. When the ratio of

Sn^{4+} to Sn^{2+} is 1:1, a uniform, compact, and noncracking CZTSSe thin film is obtained, effectively alleviating the interface recombination and reducing the concentration of deep level defects. In particular, the concentration of Cu_{Zn} antisite defects is decreased by an order of magnitude, and the carrier recombination and band tail effect are alleviated. When J_{SC} is maintained, V_{OC} and *FF* are considerably improved. Finally, we fabricate CZTSSe thin film solar cells with efficiency of over 11%. This work demonstrates the feasibility of controlling the ratio of Sn^{4+} to Sn^{2+} in the CZTSSe precursor solution for higher efficiency of CZTSSe thin film solar cells.

1. Introduction

In recent years, kesterite ($Cu_2ZnSn(S,Se)_4$, CZTSSe) semiconductors have attracted increasing attention because they own nontoxic and earth-abundant contents, outstanding absorption coefficient (>10^4 cm^{-1}), appropriate optical band gap (1.0–1.5 eV), and high theoretical efficiency (32%–34%).[1-6] Thus, they have great potential to replace $Cu(In,Ga)Se_2$ (CIGS) and CdTe solar cells. Numerous studies have shown that the fabrication of CZTS absorption layer can be achieved using various vacuum and nonvacuum technologies. The vacuum preparation method has the advantages of accurately controlling the film thickness, less elemental impurities, and feasible large-area production. Currently, the commonly used vacuum methods include sputtering,[7-10] evaporation,[11-14] and pulsed laser deposition.[15-17] For example, Yan et al. obtained 11.01% efficient Cu_2ZnSnS_4 solar cells via co-sputtering Cu/ZnS/SnS materials with the heterojunction heat treatment.[18] Li et al. achieved $Cu_2ZnSnSe_4$ solar cells with

11.95% efficiency fabricated by sputtering a Cu–Zn–Sn–Se quaternary compound target.[9] Nevertheless, to date, CZTSSe solar cells with the highest power conversion efficiency (12.6%) was performed using a hydrazine-based pure solution approach.[19] Compared with the vacuum preparation method, the solution method has received an increasing interest for the following reasons: (1) low cost, (2) few element volatilization, (3) simple experimental apparatus, (4) easily adjusted proportion of elements in the film, and (5) uniform mixing of elements in the solution, thereby reducing secondary phases.[2,4] For the solution method, the selection of tin ions (including Sn^{2+} and Sn^{4+}) is extremely vital in the precursor solution. Many groups used precursor solutions containing Sn^{2+} prepared by $SnCl_2 \cdot 2H_2O$ to fabricate CZTS precursor films.[20-24] Generally, the preparation of Sn^{2+} solution can be performed in air environment, and the obtained precursor films have good compactness. However, this solution formula is faced with the problem of film cracking, which requires additives, such as monoethanolamine (MEA) and triethanolamine (TEA), to improve the viscosity, stability, and reactivity of solution.[25] Thus, the adhesion between the solution and substrate is enhanced, and the cracking of film is greatly inhibited. Although adding additives provides these benefits, the CZTS precursor films inevitably contain more organic impurities, such as carbon and oxygen, resulting in severe degradation of device performance. Hence, Sn^{4+} is introduced. Xin et al. obtained 12.4% efficiency of CZTSSe solar cells via Sn^{4+} with a record low $V_{oc\text{-}def}$ of 0.297 V. They revealed two different grain growth mechanisms of Sn^{2+} and Sn^{4+} precursor films; thus, the open-circuit voltage deficit remarkably differs. Compared with Sn^{2+} precursor films, Sn^{4+}

precursor films own direct phase transformation grain growth mechanism in the selenization process, which can avoid $SnSe_2$ secondary phases and greatly suppress the formation of detrimental deep defects.[26, 27] However, anhydrous $SnCl_4$ was used as tin source for preparing Sn^{4+} precursor films. Precursor solution preparation in the glove box is necessary, to greatly increase the complexity of experimental operation given the volatile nature of anhydrous $SnCl_4$.

We used $SnCl_4 \cdot 5H_2O$ powder to replace anhydrous $SnCl_4$ to prepare Sn^{4+} precursor solution in air environment, considering all these factors. However, the quality of the obtained absorption layer was not improved, and the devices became inefficient due to many holes. In view of the good compactness of the precursor film fabricated by Sn^{2+}, we mixed two different precursor solutions containing Sn^{2+} and Sn^{4+} as the final precursor solution, and the effects of the ratio of Sn^{4+} to Sn^{2+} precursor solutions on the performance of CZTSSe thin films and devices were systematically investigated. We have not only simplified the experiments, but also rendered a feasible scheme to obtain denser precursor films and avoid film cracking. Finally, we found that a 1:1 ratio of Sn^{4+} to Sn^{2+} presented better performance by taking full advantage of Sn^{2+} and Sn^{4+}, and the best efficiency of 11.1% was obtained.

2. Results and Discussion

Figure 1a shows the X-ray diffraction (XRD) patterns of CZTSSe thin films with different ratios of Sn^{4+} to Sn^{2+}, corresponding to 1:0, 2:1, 1:1, 1:2, and 0:1. It should be noted that the ratio of Sn^{4+} to Sn^{2+} indicates the mole ratio of $SnCl_4 \cdot 5H_2O$ (Sn^{4+}) to

$SnCl_2 \cdot 2H_2O$ (Sn^{2+}) in the precursor solution, rather than the ratio of Sn^{4+} to Sn^{2+} in the solution after reaction. The definition (the ratio of Sn^{4+} to Sn^{2+}) strictly followed throughout this work. The diffraction peaks of the characteristic (110) planes of Mo substrate were located at $2\theta = 40.4°$, whose signals were weak due to thicker CZTSSe absorption layers or $MoSe_2$ layers. Three major diffraction peaks of (112), (204), and (312) of CZTSSe could be easily observed, and especially (112) crystal planes showed strong and sharp characteristics, indicating the high crystalline nature of CZTSSe thin films.[27, 28] At the same time, the variation of the full width at half maximum (FWHM) of (112) plane for CZTSSe samples with diverse ratios of Sn^{4+} to Sn^{2+} is presented in the inset image of Figure 1a. The FWHM of the CZTSSe thin film, whose ratio of Sn^{4+} to Sn^{2+} was 1:1, was the smallest, suggesting that the thin film has the best crystallinity under this ratio.[22] This finding may be on account of the smallest contact angle of the precursor solution with 1:1 of Sn^{4+} to Sn^{2+} on the Mo substrate at 7.1°, and the two other contact angles were 7.9° and 8.6°, corresponding to the pure Sn^{4+} and Sn^{2+} precursor solutions, respectively **(Figure S1)**. The surface free energy can be calculated using the liquid contact angle by the Young–Dupre equation, as follows:

$$W = \gamma(1 + cos\theta) \quad (1)$$

where w is the surface free energy (N/m), γ is the surface tension of liquid, and θ is the contact angle.[29] An inverse relationship is found between the value of the liquid contact angle and the surface free energy. If the contact angle θ is smaller, then the surface free energy is larger. The higher surface free energy indicates better wetting of hydrophilic materials; this condition is conducive to the growth of the precursor films

and the reduction of stress.[30-32] The specific values of the grain size were discussed in detail in AFM characterization. In addition, other CZTSSe peaks were located between the peaks of the standard kesterite $Cu_2ZnSnSe_4$ and Cu_2ZnSnS_4 phases, according to JCPDS standard card CZTSe No. 052–0868 and CZTS No. 026–0575. The XRD patterns showed no additional peaks of secondary phases for CZTSSe thin films with different ratios of Sn^{4+} to Sn^{2+}.

On the basis of the XRD pattern analysis, Raman spectroscopy measurement was further performed to more accurately identify the secondary phases in the CZTSSe semiconductor, such as $Cu_2Sn(S,Se)_3$, Zn(S,Se), Sn(S,Se), and $Sn(S,Se)_2$. As shown in Figure 1b, one significant main peak at approximately 207 cm^{-1} corresponded to the A_1 vibration mode of CZTSe, originating from the vibration of selenium atoms surrounded by other atoms in the lattice. Moreover, the Raman peak of 330 cm^{-1} can be ascribed to the A vibration mode of CZTS, and the frequency of A mode mainly depends on the sulfur atom vibration. These vibration modes are the bimodal behavior of $Cu_2ZnSn(S,Se)_4$ alloy. The minor peaks at approximately 180 and 243 cm^{-1} can correspond to B and E modes of CZTSSe, respectively.[33] In summary, combining the results of XRD and Raman characterization, no redundant secondary phases could be detected in the CZTSSe thin films prepared by mixing two different precursor solutions with Sn^{4+} and Sn^{2+}.

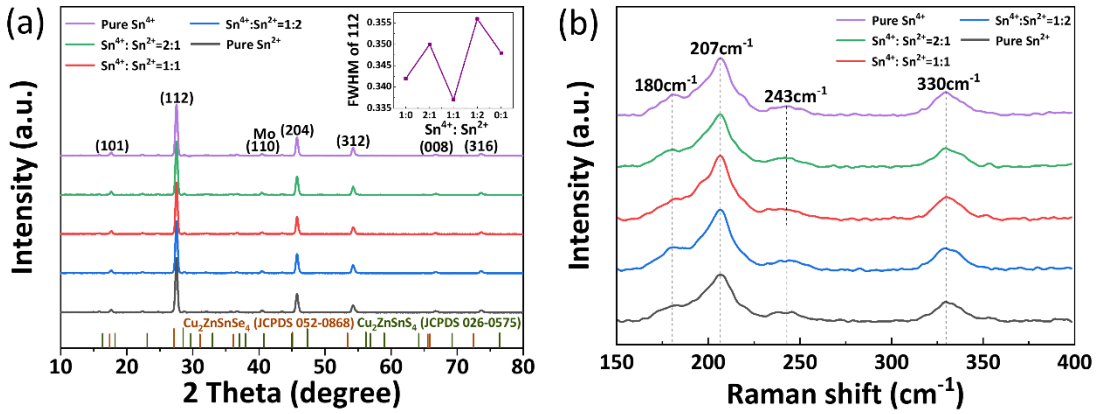

Figure 1. XRD patterns (a) and Raman spectra (b) of the CZTSSe thin films obtained from different ratios of Sn^{4+} to Sn^{2+} precursor solutions. The inset in (a) shows the comparison of FWHM of the (112) plane.

Figure 2 shows the surface scanning electron microscope (SEM) images of the precursor and selenized CZTSSe films with different ratios of Sn^{4+} to Sn^{2+}, and the cross-sectional images of the corresponding devices. Evidently, the CZTS thin film prepared by pure Sn^{2+} precursor solution was cracked. Other precursor films with different ion ratios showed flat and smooth surface without cracks. The problem of film cracking was solved successfully by mixing two different precursor solutions containing Sn^{4+} and Sn^{2+}. Notably, many pinholes were found on the surface of the CZTSSe thin film with pure Sn^{4+} in accordance with its cross section, which was sign of poor compactness. The pinholes may result from easier decomposition of the CZTSSe thin film during selenization. Figures 2-b2, c2, and d2 exhibit compact morphology with large grains, accompanying some small grains sprinkled on the surface. However, a denser film surface with larger grain size than the two other films is shown in Figure 2-d2, implying that the precursor solution containing more Sn^{2+}

(with a 1:2 ratio of Sn^{4+} to Sn^{2+}) was effective in obtaining more compact selenized film. The cross-sectional morphologies of CZTSSe devices with different ratios of Sn^{4+} to Sn^{2+} were presented in Figures 2(a3–e3). All devices presented a three-layer sandwich structure that the middle fine-grained layer was sandwiched between the top and bottom large grains. Regardless of the CZTSSe crystalline structure, fine grains were inevitable in most cases and may be derived from high carbon residual.[21] In these three-layer structures, grain size and density varied considerably. With the increase of Sn^{2+} concentration, the top grain size increased significantly. Compared with devices C, D and E, the CZTSSe crystals of devices A and B showed a more loosely stacked structure with many holes due to more Sn^{4+} in the precursor solution. The performance of solar cells would be poor because more grain boundaries and voids lead to severe recombination of photon-generated carriers. The larger top grains and denser middle fine-grained and bottom large grain layers of device E with pure Sn^{2+} precursor solution were obtained contrary to the loose and porous structure of device A with pure Sn^{4+} solution. This finding indicates the positive effects of Sn^{2+} on forming more compact thin films after selenization. However, device E had a large hole in the absorber. Few large holes may form in some cracked areas during selenization due to the initial precursor film cracking. The cross-sectional image of the champion device C exhibited the densest absorption layer with the least voids. The grain size of fine crystallized layer was larger than those of other devices; it was vital to the device performance. Sn^{2+} plays an important role in influencing the compactness of the selenized films. Xin et al. demonstrated the benefits of direct phase transformation grain growth mechanism of

Sn^{4+} film, that is, this growth mechanism can avoid $SnSe_2$ secondary phases and greatly suppress the formation of detrimental deep defects.[27] For device C with 1:1 of Sn^{4+} to Sn^{2+}, the two ions were "neck and neck" in the mixed precursor solution. Hence, device C took full advantage of Sn^{2+} and Sn^{4+} and formed preferable thin film by analyzing the cross section. Meanwhile, the back contact layer of $MoSe_2$ could be observed in all devices whose thickness varied from approximately 300–500 nm. In CZTSSe solar cells, the $MoSe_2$ layer with appropriate thickness is beneficial to enhancing the adhesion between the layers, forming ohmic back contact. Otherwise, layer separation of thin films and an increase in series resistance would be induced by too thick $MoSe_2$.

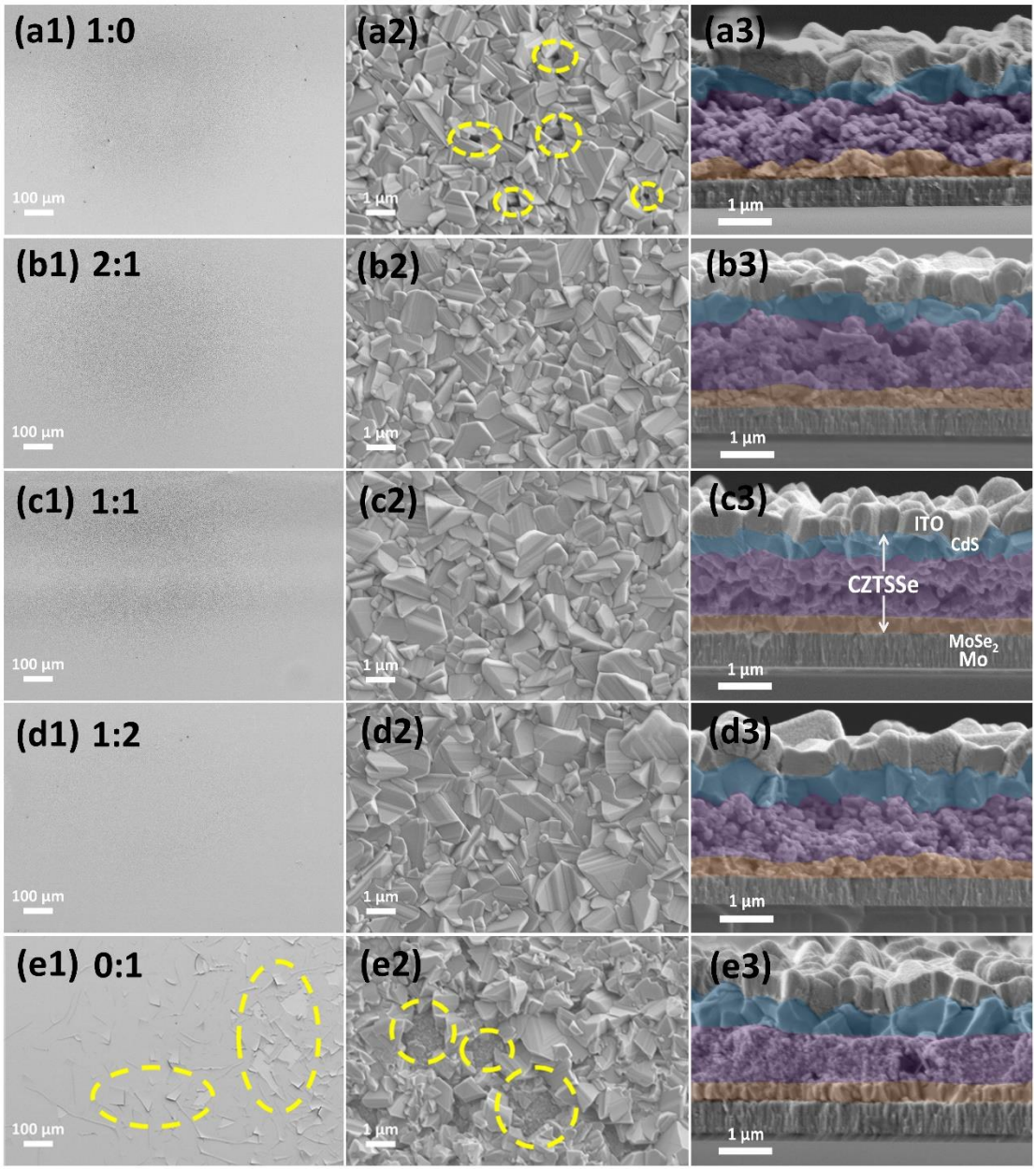

Figure 2. The surface SEM images of CZTSSe thin films (a1-e1, a2-e2) obtained from different ratios of Sn^{4+} to Sn^{2+} and the cross-sectional images (a3-e3) of the corresponding devices (devices A~E). The CZTSSe absorbers were marked in three different colors in a3-e3. "A, B, C, D, E" and "a, b, c, d, e" correspond to 1:0, 2:1, 1:1, 1:2, and 0:1 of Sn^{4+} to Sn^{2+} precursor solutions respectively.

AFM (Atomic force microscope) was performed further to study the topography,

surface average roughness, and grain size of CZTSSe thin films with the three ratios (1:0, 1:1 and 0:1) of Sn^{4+} to Sn^{2+}, as shown in **Figure 3**. To investigate the individual effects of Sn^{4+} and Sn^{2+} on the film quality and their combined effects, so only three representative ratios were compared here. Topographies (a) and (b) observed from AFM 2D views were consistent with the top-view SEM images (a2) and (c2), but topography (c) corresponds to the no cracking portion of the pure Sn^{2+} CZTSSe thin film. The AFM surface topography was combined with the corresponding fitted grain map, and (b) and (e) show larger surface grains, and (c) and (f) present more compact surface with many uniformly sized grains relative to (a) and (d) with some visible pinholes. This finding could also be verified by the histogram of the max grain average size and the min grain average size. The average values of the average size of all detected grains were 0.562 , 0.589 , and 0.561 μm. In addition, the histogram of average roughness shows that the CZTSSe thin film with 1:1 of Sn^{4+} to Sn^{2+} has a minimal average roughness of 88.18 nm. When the ratios of Sn^{4+} to Sn^{2+} was 1:0 and 0:1, the average roughness was 91.46 and 99.26 nm. According to the literature,[30, 33-37] the rough CZTSSe films have a comparatively high number of defects in the heterojunction region, which acts as an interfacial recombination center. The smaller roughness indicates the better film surface quality of absorption layer, which is beneficial for the growth of the much better and more uniform CdS film with the same chemical bath deposition (CBD) process, showing superior heterojunction quality.[30, 38, 39] The interfacial defect concentration decreases, and the interface recombination has been effectively suppressed.

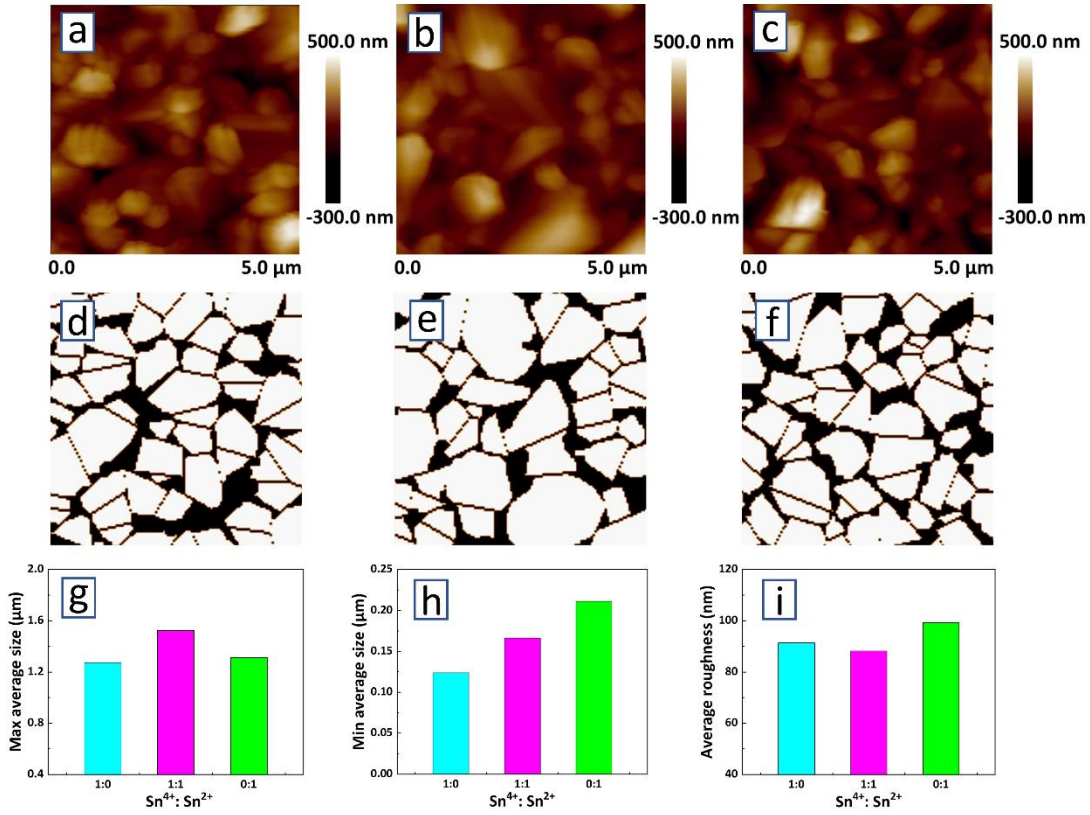

Figure 3. a-c) AFM topography images of CZTSSe thin films corresponding to 1:0, 1:1, and 0:1 of Sn^{4+} to Sn^{2+}. d-f) The fitted grain map according to the AFM topography images (a-d, b-e, c-f). g) The histogram of the max average size. Max average size means the average size of the largest grain detected. h) The histogram of the min average size. Min average size means the average size of the smallest grain detected. i) The histogram of average roughness of CZTSSe thin films.

The statistical average device performance parameters reflecting photovoltaic properties are shown in **Figure 4**, including power conversion efficiency (PCE), open-circuit voltage (V_{OC}), fill factor (*FF*), and short-circuit current density (J_{SC}). The figure confirms the reliability and reproducibility of device preparation process with our mixed solution formula. Evidently, the devices show the highest average efficiency

when the ratio of Sn^{4+} to Sn^{2+} was 1:1 because the best V_{OC} and *FF* (507 mV and 69.91%, respectively) were obtained under this condition. This result indicates better interfaces whether between the absorption layer and Mo back electrode or CdS layer and highly crystalline thin film via XRD and SEM analyses. Thus, the concentrations of bulk and interfacial defects were reduced, and the recombination was effectively suppressed. Furthermore, high concentration defects could produce undesirable band tail effect and limit the lifetime of minority carriers.[6, 19, 26, 40, 41] Short-circuit current density of solar cells with five ratios, apart from 0:1, was comparable. Apparently, the devices with pure Sn^{2+} had unsatisfactory performance in all photovoltaic parameters owing to the film cracking.

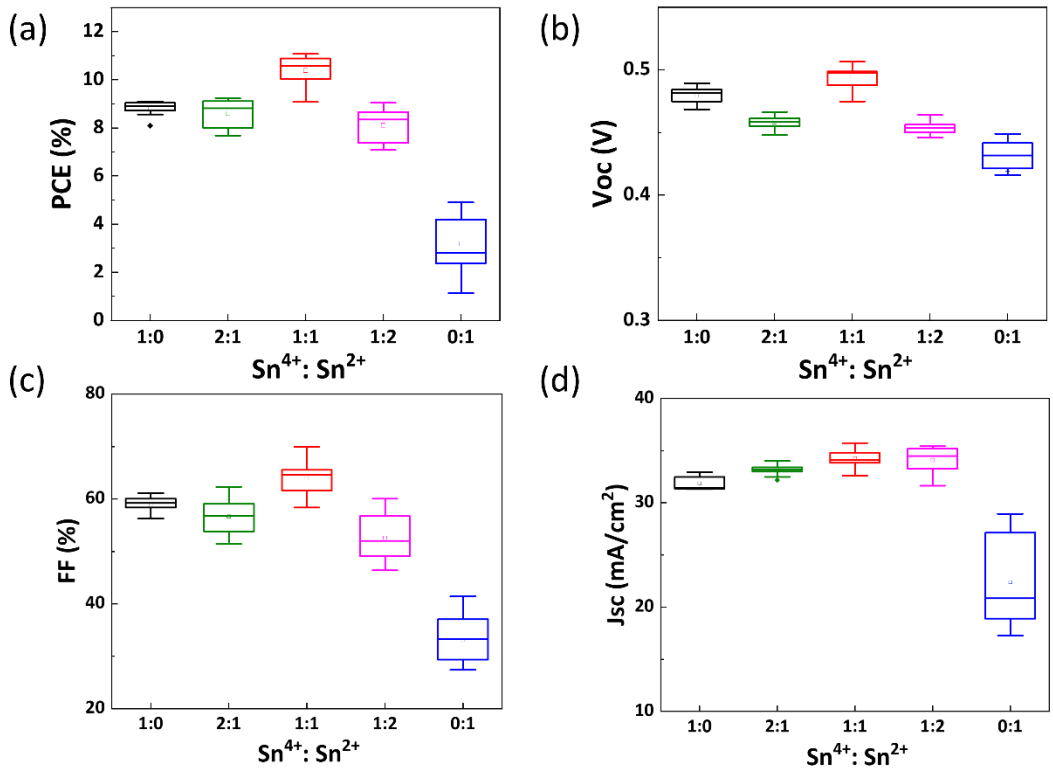

Figure 4. The statistical distribution of the device photovoltaic parameters including a) power conversion efficiency (PCE), b) open-circuit voltage (V_{OC}), c) fill factor (*FF*), d)

short-circuit current density (J_{SC}) under the ratios of 1:0, 2:1, 1:1, 1:2, and 0:1 of Sn^{4+} to Sn^{2+}.

In particular, the best-performing current–voltage (*J–V*) characteristics of the CZTSSe solar cell with 1:1 of Sn^{4+} to Sn^{2+} measured in the dark and under AM 1.5 G illumination is shown in **Figure 5**a. More intuitively, the *J–V* curves and corresponding device parameters of the best devices with 1:0, 1:1, and 0:1 of Sn^{4+} to Sn^{2+} are presented in Figure 5b. Device E had a poor performance in V_{OC}, J_{SC}, and *FF* and had the lowest efficiency among the three devices because of the cracking of the CZTS precursor films with pure Sn^{2+}. Evidently, device C had advantages in the V_{OC} and *FF* given that V_{OC} was enhanced from 482 mV to 507 mV, and *FF* was increased from 58.34% to 65.36% compared with device A. This finding may be attributed to the reduced interfacial defect and deep-level defect concentrations.

The external quantum efficiency (EQE) was also measured to obtain the optical response of CZTSSe devices, as shown in Figure 5c with corresponding integrated J_{SC}. Device C clearly exhibited a higher optical response over the entire wavelength range (from 300 nm to 1200 nm), indicating that device C had better carrier collection efficiency than devices A and E, and a lower recombination of photon-generated carriers was in the CZTSSe bulk and at the interface between the absorption layer and Mo substrate.[22, 23] EQE was over 90% in the wavelength range from 525 nm to 690 nm for device C. Furthermore, the band gap of CZTSSe absorber in these devices was determined by plotting d(-ln(1-EQE)) versus dE. According to Figure 5d, the band-gap

value of devices A and C was approximately 1.2 eV and approximately 1.25 eV for device E. Figures 5e and 5f show the Urbach tail model to characterize the variation in the band tail states. The ln(-ln(1-EQE)) versus energy plot extracted the Urbanch energy of the devices from the inverse of the slope for the linear portion below the bandgap;[23] the values were 28.49, 26.14, and 28.94 meV for devices A, C, and E, respectively. Minimal Eu was obtained for device C, demonstrating a reduction in band tail effect.

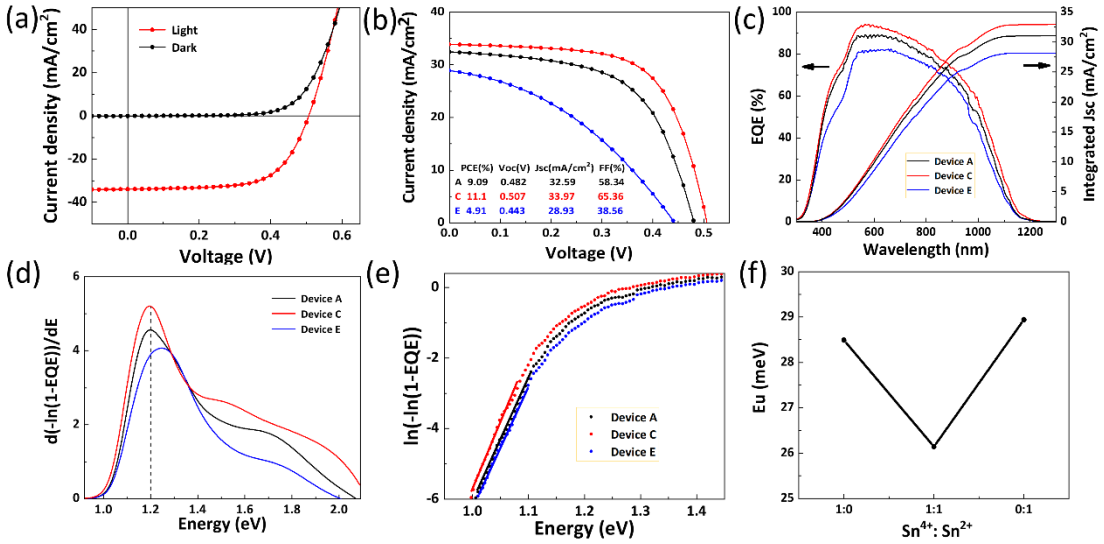

Figure 5. a) *J–V* curves of the champion CZTSSe solar cell (device C) measured in the dark and under AM 1.5 G illumination; b) *J–V* curves of devices A, C, and E corresponding to 1:0, 1:1, and 0:1 of Sn^{4+} to Sn^{2+}, respectively; c) EQE spectra and the corresponding integrated J_{SC} of devices A, C, and E; d) The band gaps were determined by the d(-ln(1-EQE))/dE versus E curves; e) ln(-ln(1-EQE)) vs energy plot to show the band tail states; f) The variation of the Urbach values of devices A, C and E.

Diode performance parameters reflecting junction-dependent electrical behavior were systematically investigated to study the recombination mechanism of solar cell. When

a voltage was applied to the solar cells in the dark conditions, the solar cells exhibited the diode rectification characteristics shown in the **Figure 6**a. Thereafter, shunt conductance (G), series resistance (R), diode ideality factor (A), and reverse saturation current density (J_0) were calculated according to the general single exponential diode equation,[42, 43] as follows:

$$J = J_0 \exp\left[\frac{q}{AkT}(V - RJ)\right] + GV - J_L \quad (2)$$

where J_L is light current density. The shunt conductance G values, 1.2 and 0.5 mS/cm^2, were obtained by making a tangent to the flat region under reverse bias, where it intersects the Y-axis in Figure 6b. The series resistance R is the intercept of Y-axis, and the diode ideality factor A, which is the most important sign to measure the quality of p-n junction, could be calculated from the slope of AkT/q in the plot of dV/dJ against $(J+J_{SC})^{-1}$ (Figure 6c). The R and A of device A were 1.86 Ω cm^2 and 2.59, respectively. High A ($A > 2$) value reveals serious Shockley–Read–Hall recombination (depletion region) of device A, which may be from the high defect concentrations on/near the absorber surface.[27] On the contrary, the values decreased to 0.84 Ω cm^2 and 1.88 for device C, suggesting better p-n junction quality and improved interface recombination. The decrease in the series resistance may contribute to the increased *FF*. The reverse saturation current density J_0 was deduced from the Y-intercept $\ln J_0$ by plotting ln(J+Jsc-GV) against V-RJ (Figure 6d), which was 4.25×10^{-2} and 9.13×10^{-4} mA/cm^2 for devices A and C, respectively. A smaller reverse saturation current density indicates better unilateral conductivity of the diode and closer to the ideal transistor. In summary,

device C had superior diode performance parameters to device A, indicating improved heterojunction quality of CdS/CZTSSe.

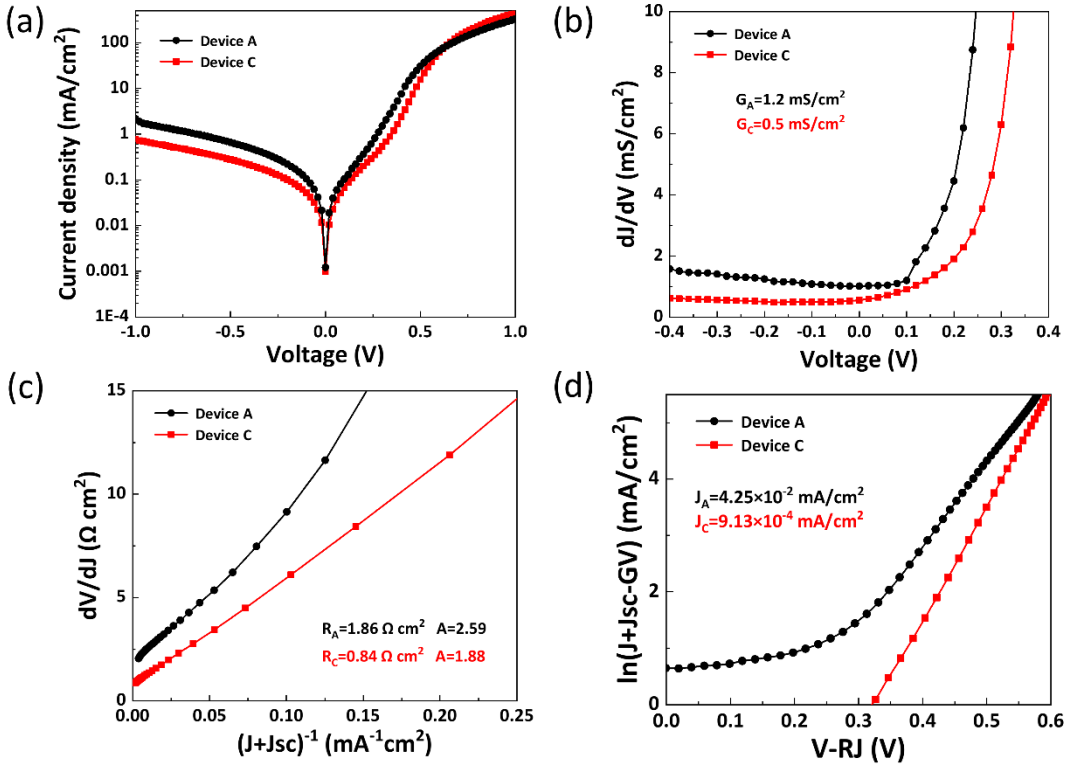

Figure 6. Electrical behaviors of the representative devices A and C with 1:0 and 1:1 of Sn^{4+} to Sn^{2+}: a) Dark J-V curves; b) Shunt conductance *G* characterization; c) Series resistance *R* and ideality factor *A* characterization; d) Reverse saturation current density J_0 characterization.

In addition, the charge densities in the CZTSSe absorption layers of devices A and C were probed by the capacitance-voltage (*C–V*) and drive level capacitance profiling (DLCP) measurements, and the relevant results are shown in **Figure 7**a and **Table 1**. According to literature,[7, 24, 44] N_{CV} includes bulk defects, interfacial defects, and free carriers, and N_{DL} comprises bulk defects and free carriers. Therefore, the difference between N_{CV} and N_{DLCP} (N_{CV}-N_{DL}) at zero bias reflects the defect states at the

CZTSSe/CdS interface, i.e., the interfacial defect density. The plots of N_{CV} and N_{DL} against x present two phenomena, as follows: (1) the N_{CV} and N_{DL} of device C were less than those of device A; (2) the depletion width of device C was wider than that of device A. These findings are valid because the CZTSSe devices with high charge density generally correspond to narrow depletion width, which is consistent with previous reports.[24] Specifically, the values of N_{DL} for devices A and C were 1.22×10^{16} and 6.36×10^{15} cm^{-3}, respectively, and the free carrier concentrations should be similar because their absorption layers own similar chemical compositions with the same stoichiometric ratio of the solution.[27] Hence, more deep-level defects were in device A, which was analyzed in the subsequent DLTS results. Furthermore, the interfacial defect densities of devices A and C were 3.57×10^{15} and 1.39×10^{15}, respectively, in virtue of N_{CV}-N_{DL} (N_{IT}). The reduction of N_{IT} (at zero bias) indicated the decrease in interface traps. Thus, the interface recombination and device performance degradation induced by surface states were suppressed. This finding also dovetailed effectively with SEM images (Figure 2); device C presented better film quality in the surface or cross section of CZTSSe absorber. The depletion region is equivalent to an insulating layer, where the mobile charge carriers have diffused away, and it is beneficial to separate electron-hole pairs with the wider depletion layer, which is closely related to the conductivity of charge carriers.[24, 45, 46]

Table 1. Summary of the results derived from *C-V* and DLCP measurements.

Device	N_{CV} [cm^{-3}]	N_{DL} [cm^{-3}]	Depletion width [nm]	Interface state response (relative values)

Device-A	1.57×10^{16}	1.22×10^{16}	149	3.57×10^{15}
Device-C	7.75×10^{15}	6.36×10^{15}	170	1.39×10^{15}

To obtain a more objective understanding of the defects in devices A and C, capacitance-mode deep-level transient spectroscopy (C-DLTS) was performed on these devices to quantify the trap activation energy (E_a), trap concentration (N_T), and capture cross section (σ_T) of the deep level defects given that *C–V* and DLCP cannot directly reflect deep-level defect concentrations and types. The C-DLTS spectra are shown in Figure 7b. The two peaks in one curve (device C) and three peaks in another curve (device A) indicate that one more detected deep-level defect exists in device A. As shown in Figure 7c, the Arrhenius plots deduced from the corresponding peaks of DLTS spectra presents different trap activation energies, and the detailed defect parameters of these devices are summarized in **Table 2**. The defect activation energy extracted from the Arrhenius plot is the energy difference between the valence band edge and the defect level.[47] Generally, the acceptor defect with E_a in the range of 0.1–0.2 eV can be ascribed to Cu_{Zn} antisite defects and that of 0.25–0.42 eV can be assigned to the Cu_{Sn} antisite defect on the basis of theoretical calculation with respect to the defects of kesterite CZTSSe solar cells.[48-50] Therefore, the defects with E_a of 0.108 and 0.168 eV corresponded to Cu_{Zn} antisite defect, and those with E_a of 0.318 and 0.393 eV corresponded to Cu_{Sn} antisite defect via analyzing the defect activation energy and the defect formation energy. On the contrary, device C had lower trap activation energy, indicating that device C has shallower defect level. Figure 7d demonstrates that the positions of the defect that E_{a1} and E_{a2} in devices A and C are relative to the valence

band maximum (VBM).[51-53] In addition, device C obtained a relatively faster emission rate, according to the following formula of the emission rate of carrier:

$$R_{emission} = \sigma \upsilon N exp(-\frac{E_a}{kT}) \quad (3)$$

where σ is the carrier capture cross section, υ is the mean thermal velocity, and N is the effective density of state; thus, carrier recombination could be alleviated.[54]

Table 2. Defect properties of devices A and C measured by C-DLTS.

Device	Peak	Temperature [K]	Activation energy E_a [eV]	trap conc. N_T [cm^{-3}]	Possible defect
Device-A	Peak 1	193	0.168	6.05×10^{14}	Cu_{Zn}
	Peak 2	243	0.393	2.86×10^{12}	Cu_{Sn}
	Peak 3	298	0.691	4.10×10^{11}	V_{Sn}
Device-C	Peak 1	116	0.108	2.64×10^{13}	Cu_{Zn}
	Peak 2	297	0.318	1.68×10^{12}	Cu_{Sn}

The concentration of Cu_{Zn} and Cu_{Sn} antisite defects has been effectively inhibited in device C. In particular, the N_T of Cu_{Zn} defect in device C was one order of magnitude lower than that in device A, which was 2.64×10^{13} and 6.05×10^{14} cm^{-3}. Cu_{Zn} defect is always the dominant defect in the stable chemical potential region. The two main reasons are as follows: (1) the formation energy of Cu_{Zn} antisite defect is lower than those of other defects, including V_{Cu}; (2) Cu and Zn have similar atomic number and size (Cu, Zn≈1.35 Å). However, Cu_{Zn} antisite defects are detrimental to device performance because they act as carrier recombination centers. Photon-generated electrons could be trapped on the deep defect levels, which not only influence the minority carrier lifetime, but also the electrical conductivity and series resistance.

Therefore, the open-circuit voltage and fill factor are limited.[47, 51] Meanwhile, one point that should not be neglected is that the acceptor defect Cu_{Zn} can unite donor defects, such as Zn_{Cu} and Sn_{Zn}, to form Cu_{Zn}+Zn_{Cu}, Cu_{Zn}+Sn_{Zn}, and 2Cu_{Zn}+Sn_{Zn} defect clusters.[55] Accordingly, the reduction of Cu_{Zn} defects could inhibit the formation of these defect clusters, which may alleviate band tail effect, band gap and electrostatic potential fluctuations. As a result, V_{OC} increases due to the few recombination of carriers.[52, 53] Therefore, device A performed worse than device C under the condition of the comparable short-circuit current density. In addition, the very deep defect with E_{a3} of 0.691 eV may be V_{sn}, whose concentration is in the order of 10^{11}, which is far below the usual defects to be negligible.

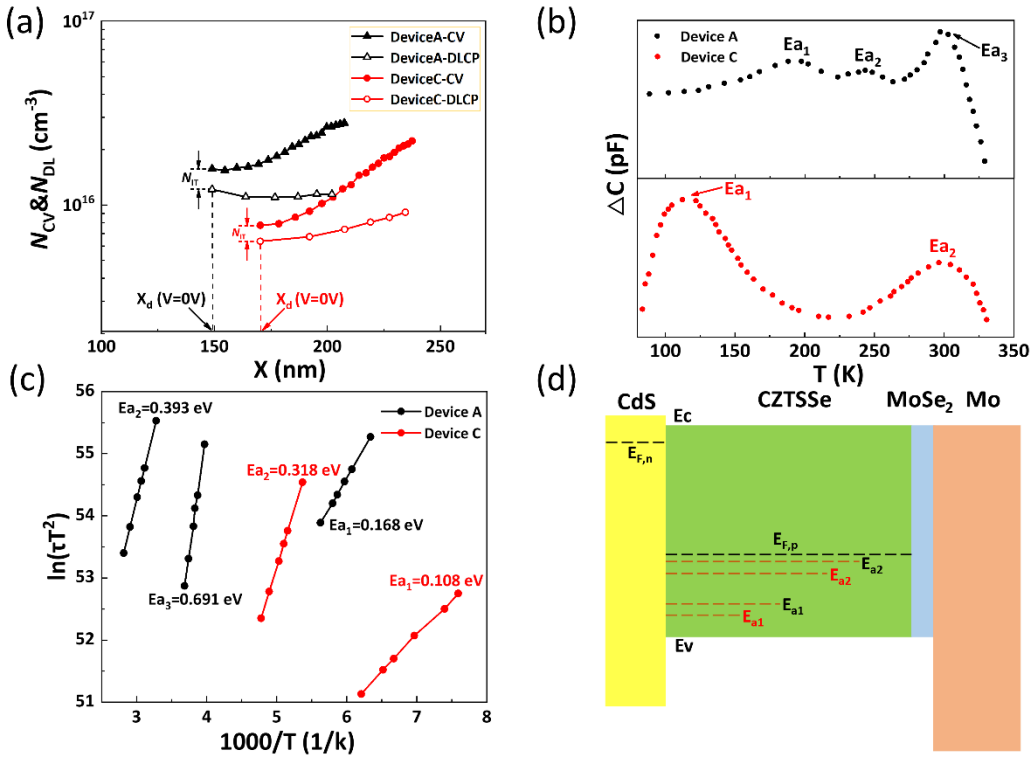

Figure 7. a) The *C-V* and DLCP profiles of devices A and C; b) C-DLTS signals of devices A and C; c) Arrhenius plots corresponding to the peaks derived from DLTS

spectra; d) Schematic diagram of the band energy and the defect energy level of the devices A and C.

3. Conclusion

Anhydrous $SnCl_4$ was substituted with $SnCl_4 \cdot 5H_2O$ powder to prepare Sn^{4+} precursor solution in air environment for the first time. Then, the proportion of Sn^{4+} and Sn^{2+} in the solution was controlled by mixing two different precursor solutions containing Sn^{2+} and Sn^{4+} as the final precursor solution. In addition, the influence of different ratios of Sn^{4+} to Sn^{2+} on the morphology of the films was further systematically studied. We not only simplified the experiments, but also rendered a feasible scheme to obtain denser precursor film and avoid film cracking. Combining XRD, surface SEM images of the CZTSSe thin films, and cross-sectional images of corresponding devices, we found that a more uniformly compact and noncracking CZTSSe thin film could be obtained by taking full advantage of Sn^{2+} and Sn^{4+} when the ratio of Sn^{4+} to Sn^{2+} was 1:1. The interface recombination of the devices with 1:1 of Sn^{4+} to Sn^{2+} was effectively suppressed according to *C-V* and DLCP analyses because of the better quality of absorbers. The DLTS results show that the concentrations of deep-level defects were also reduced. Especially, the concentration of Cu_{Zn} antisite defects was decreased by an order of magnitude, and thus the carrier recombination and band tail effect were improved, thereby significantly elevating the open-circuit voltage and the filling factor. Hence, the photoelectric conversion efficiency of 11.1% for kesterite CZTSSe thin film solar cells was obtained. Although the film morphology made by 1:1 is the best among the five ratios, it is still not the most ideal absorption layer morphology, namely, single-

layer CZTSSe crystals. Thus, the interface defects and deep-level defects have been insufficiently decreased. The ideal CZTSSe absorption layer can be obtained by exploring a better precursor solution formula or improving other processes to achieve higher device efficiency.

4. Experimental Section

4.1. Preparation of CZTS Precursor Solution

The Sn^{4+} and Sn^{2+} precursor solutions were prepared by dissolving CuCl, $Zn(CH_3COO)_2 \cdot 2H_2O$, $SnCl_4 \cdot 5H_2O$, and $SC(NH_2)_2$ and $Cu(CH_3COO)_2 \cdot H_2O$, $ZnCl_2$, $SnCl_2 \cdot 2H_2O$, and $SC(NH_2)_2$ into 2-Methoxyethanol, respectively, then stirring them at 60 °C for approximately 1 hour to obtain a dark yellow solution. The ratios of Cu/(Zn+Sn) and Zn/Sn in the solution were 0.775 and 1.2, respectively. The precursor solution was diluted to half of its original concentration, and the ratios of Sn^{4+} and Sn^{2+} in the solution were obtained by uniformly mixing the precursor solutions containing Sn^{4+} and Sn^{2+} in different proportions.

4.2. Fabrication of CZTSSe Thin Film

The CZTSSe precursor films were deposited on molybdenum (Mo)-coated soda–lime glass (Mo-SLG) substrates via spin coating method, and spin coating was repeated 10 times with 3000 rpm for 20 s followed by preheating at 280 °C for 2 min on a hot plate in air. Subsequently, the annealing process was adopted for precursor thin films under selenium atmosphere to obtain CZTSSe thin films. The CZTS precursor films together with selenium granules were placed into a sealed graphite box, annealed at 555 °C for

15 min in pure Argon flow with different heating-up process in a rapid thermal processing furnace, and then cooled down naturally with the furnace. The quartz tube containing the sample and selenium granules was purged three times by Argon prior to selenization.

4.3. Device Fabrication

Cadmium sulfide buffer layer with approximately 60 nm thickness was deposited on selenized CZTSSe thin films by using chemical bath deposition (CBD). The CBD solution contained $CdSO_4$ (0.015 M, 20 mL), thiourea (0.75 M, 20 mL), ammonia (14.8 M, 20 mL), and deionized water (140 mL). The CBD process was maintained for 9 min at 80 °C. Then, the ITO thin films were directly sputtered on CdS/CZTSSe/Mo/glass by RF magnetron sputtering under suitable O_2/Ar ratio atmosphere (O_2/Ar ≈ 2%) at 100 W working power and 0.4 Pa working pressure for 25 min. Subsequently, the top contact Ag electrodes were deposited on the ITO by thermal evaporation. Finally, the CZTSSe thin film solar cells (Ag/ITO/CdS/CZTSSe/Mo/glass) were fabricated, the area of which was 0.16 cm^2 by mechanical scribing.

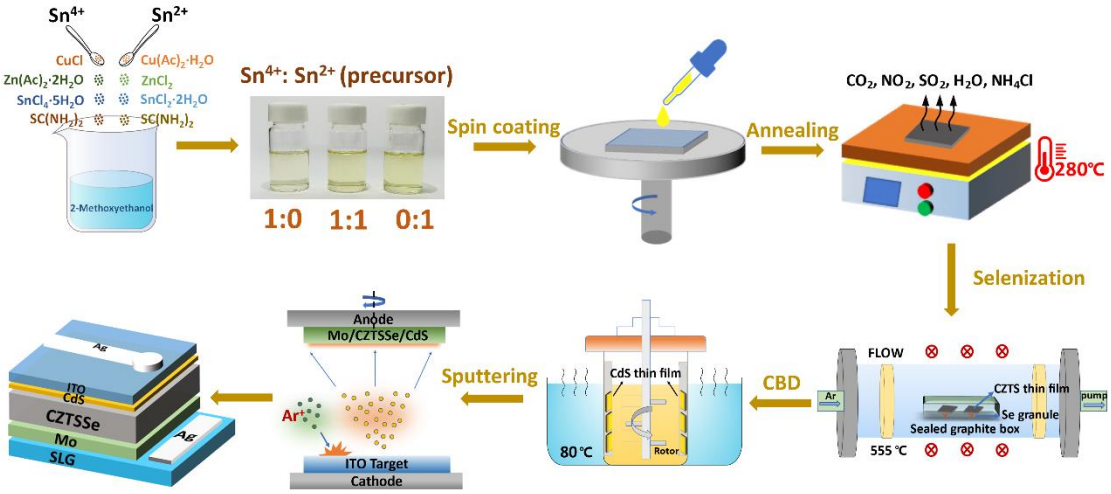

Figure 8. Schematic illustration of the fabrication process of CZTSSe thin film solar cells.

4.4. Characterization

X-ray diffraction (XRD) patterns of the absorption layers were performed on an X-ray diffractometer (Rigaku Ultima IV) with CuK_{α} as the radiation source under testing environment of 40 kV and 40 mA from 10° to 80°. Raman spectra were collected by Raman spectrometer (Renishaw inVia) with an excitation wavelength of 532 nm. The contact angles were measured by a contact angle meter (PERFECT WAM-100). The morphology of CZTSSe thin films and cross-section images of corresponding devices were obtained by SEM (SUPRA 55), and the chemical composition of the samples was analyzed by EDS (BRUKER QUANTAX 200). Atomic force microscope (AFM) measurements were conducted by NT-MDT Spectrum Instruments under the semi-contact mode. AFM images were analyzed by image analysis software (image analysis 3.5.0.18456) attached to the instruments. Dark and illuminated J–V characteristics of CZTSSe devices were measured by a Keithley 2400 meter and a Zolix SS150 solar simulator calibrated with a certified Si cell under standard test conditions (100 mW/cm^2, 25 ℃, AM1.5G). External quantum efficiency (EQE) measurements were examined by a Zolix solar cell QE/IPCE measurement system (Solar Cell Scan 100) with calibrated Si and InGaAs photodiodes as references. Capacitance–voltage (*C–V*) profiling and drive level capacitance profiling (DLCP) were measured by a Keithley 4200A-SCS system with JANIS cryogenic platform. The *C–V* measurements were performed at AC amplitude of 30 mV and frequency of 200 kHz under a dark condition at room

temperature, with DC bias voltage from −0.5 V to 0.1 V. The DLCP was conducted with an AC amplitude from 20 mV to 140 mV and a DC bias voltage from −0.25 V to 0 V at the frequency of 200 kHz. The deep-level transient spectra (DLTS) were obtained by an FT-1030 HERA DLTS system configured with a JANIS VPF-800 cryostat controller. The scanning temperature was from 90 K to 330 K. The reverse bias (V_R), pulse voltage (V_p), and pulse width were set to −0.3 V, 0.2 V, and 10 ms, respectively.

Supporting Information

Supporting Information is available from the Wiley Online Library or from the author.

Acknowledgements

This work was supported by National Key R&D Program of China (No. 2018YFE0203400), National Natural Science Foundation of China (No. 62074102), Key Project of Department of Education of Guangdong Province (No. 2018KZDXM059), Science and Technology plan project of Shenzhen (JCYJ20190808153409238, JCYJ20190808120001755and 20200826143347001)

Conflict of interest

The authors declare no conflict of interest.

Received: ((will be filled in by the editorial staff))
Revised: ((will be filled in by the editorial staff))
Published online: ((will be filled in by the editorial staff))

References

[1] S. Giraldo, Z. Jehl, M. Placidi, V. Izquierdo-Roca, A. Perez-Rodriguez, E. Saucedo, *Adv Mater*. **2019**, 31, 1806692.

[2] T. Ratz, G. Brammertz, R. Caballero, M. Leon, S. Canulescu, J. Schou, L. Gutay,

D. Pareek, T. Taskesen, D. H. Kim, J. K. Kang, C. Malerba, A. Redinger, E. Saucedo, B. Shin, H. Tampo, K. Timmo, N. D. Ngyuen, B. Vermang, *Journal of Physics-Energy*. **2019**, 1, 042003.

[3] W. Shockley, H. J. Queisser, *Journal of Applied Physics*. **1961**, 32, 510.

[4] T. Todorov, H. W. Hillhouse, S. Aazou, Z. Sekkat, O. Vigil-Galán, S. D. Deshmukh, R. Agrawal, S. Bourdais, M. Valdés, P. Arnou, D. B. Mitzi, P. J. Dale, *Journal of Physics: Energy*. **2020**, 2, 012003.

[5] S. K. Wallace, Katrine L. Svane, W. P. Huhn, T. Zhu, D. B. Mitzi, V. Blum, A. Walsh, *Sustainable Energy & Fuels*. **2017**, 1, 1339.

[6] D.-H. Son, S.-H. Kim, S.-Y. Kim, Y.-I. Kim, J.-H. Sim, S.-N. Park, D.-H. Jeon, D.-K. Hwang, S.-J. Sung, J.-K. Kang, K.-J. Yang, D.-H. Kim, *Journal of Materials Chemistry A*. **2019**, 7, 25279.

[7] P. Fan, Z. Xie, G. Liang, M. Ishaq, S. Chen, Z. Zheng, C. Yan, J. Huang, X. Hao, Y. Zhang, Z. Su, *Journal of Energy Chemistry*. **2021**, 61, 186.

[8] J. Guo, S. Sun, R. Hao, L. Sun, L. Wang, B. Liu, *Journal of Electronic Materials*. **2021**, DOI: 10.1007/s11664-021-09027-y.

[9] X. Li, D. Zhuang, N. Zhang, M. Zhao, X. Yu, P. Liu, Y. Wei, G. Ren, *Journal of Materials Chemistry A*. **2019**, 7, 9948.

[10] T. Tanaka, T. Nagatomo, D. Kawasaki, M. Nishio, Q. Guo, A. Wakahara, A. Yoshida, H. Ogawa, *Journal of Physics and Chemistry of Solids*. **2005**, 66, 1978.

[11] S. Das, R. N. Bhattacharya, K. C. Mandal, *Solar Energy Materials and Solar Cells*. **2016**, 144, 347.

[12] Y. S. Lee, T. Gershon, O. Gunawan, T. K. Todorov, T. Gokmen, Y. Virgus, S. Guha, *Advanced Energy Materials*. **2015**, 5, 1401372.

[13] T. G. Sánchez, X. Mathew, N. R. Mathews, *Journal of Crystal Growth*. **2016**, 445, 15.

[14] B. Shin, O. Gunawan, Y. Zhu, N. A. Bojarczuk, S. J. Chey, S. Guha, *Progress in Photovoltaics: Research and Applications*. **2013**, 21, 72.

[15] M. Gansukh, S. López Mariño, M. Espindola Rodriguez, S. L. J. Engberg, F. M. A. Martinho, A. Hajijafarassar, N. C. Schjødt, E. Stamate, O. Hansen, J. Schou, S. Canulescu, *Solar Energy Materials and Solar Cells*. **2020**, 215, 110605.

[16] X. Jin, C. Yuan, G. Jiang, W. Liu, C. Zhu, *Materials Letters*. **2016**, 175, 180.

[17] S. A. Vanalakar, S. W. Shin, G. L. Agawane, M. P. Suryawanshi, K. V. Gurav, P. S. Patil, J. H. Kim, *Ceramics International*. **2014**, 40, 15097.

[18] C. Yan, J. Huang, K. Sun, S. Johnston, Y. Zhang, H. Sun, A. Pu, M. He, F. Liu, K. Eder, L. Yang, J. M. Cairney, N. J. Ekins-Daukes, Z. Hameiri, J. A. Stride, S. Chen, M. A. Green, X. Hao, *Nature Energy*. **2018**, 3, 764.

[19] W. Wang, M. T. Winkler, O. Gunawan, T. Gokmen, T. K. Todorov, Y. Zhu, D. B. Mitzi, *Advanced Energy Materials*. **2014**, 4, 1301465.

[20] X. Zhao, Y. Pan, C. Zuo, F. Zhang, Z. Huang, L. Jiang, Y. Lai, L. Ding, F. Liu, *Science Bulletin*. **2021**, 66, 880.

[21] Q. Yu, J. Shi, L. Guo, B. Duan, Y. Luo, H. Wu, D. Li, Q. Meng, *Nano Energy*. **2020**, 76, 105042.

[22] S. Ge, H. Gao, R. Hong, J. Li, Y. Mai, X. Lin, G. Yang, *ChemSusChem*. **2019**,

12, 1692.

[23] Z. Su, G. Liang, P. Fan, J. Luo, Z. Zheng, Z. Xie, W. Wang, S. Chen, J. Hu, Y. Wei, C. Yan, J. Huang, X. Hao, F. Liu, *Adv Mater*. **2020**, 32, 2000121.

[24] Z. Su, J. M. R. Tan, X. Li, X. Zeng, S. K. Batabyal, L. H. Wong, *Advanced Energy Materials*. **2015**, 5, 1500682.

[25] Z. Su, K. Sun, Z. Han, H. Cui, F. Liu, Y. Lai, J. Li, X. Hao, Y. Liu, M. A. Green, *J. Mater. Chem. A*. **2014**, 2, 500.

[26] Y. Gong, Y. Zhang, E. Jedlicka, R. Giridharagopal, J. A. Clark, W. Yan, C. Niu, R. Qiu, J. Jiang, S. Yu, S. Wu, H. W. Hillhouse, D. S. Ginger, W. Huang, H. Xin, *Science China Materials*. **2020**, 64, 52.

[27] Y. Gong, Y. Zhang, Q. Zhu, Y. Zhou, R. Qiu, C. Niu, W. Yan, W. Huang, H. Xin, *Energy & Environmental Science*. **2021**, 14, 2369.

[28] Y. Li, H.-X. Zhang, Y. Zhao, X.-F. Dong, T.-T. Zheng, C.-W. Wang, *Applied Surface Science*. **2020**, 516, 145872.

[29] M. E. Schrader, *Langmuir* **1995**, 11, 3585.

[30] Y. Sun, H. Guo, P. Qiu, S. Zhang, S. Wang, L. Wu, J. Ao, Y. Zhang, *Journal of Energy Chemistry*. **2021**, 57, 618.

[31] M. C. Gomes, A. C. Fernandes, B. S. Almeida, R. M. Almeida, *Journal of Materials Science*. **1995**, 30 3893.

[32] X. Zheng, J. Troughton, N. Gasparini, Y. Lin, M. Wei, Y. Hou, J. Liu, K. Song, Z. Chen, C. Yang, B. Turedi, A. Y. Alsalloum, J. Pan, J. Chen, A. A. Zhumekenov, T. D. Anthopoulos, Y. Han, D. Baran, O. F. Mohammed, E. H. Sargent, O. M.

Bakr, *Joule*. **2019**, 3, 1963.

[33] H. Guo, G. Wang, R. Meng, Y. Sun, S. Wang, S. Zhang, J. Wu, L. Wu, G. Liang, H. Li, Y. Zhang, *Journal of Materials Chemistry A*. **2020**, 8, 22065.

[34] S. K. Hwang, J. H. Park, K. B. Cheon, S. W. Seo, J. E. Song, I. J. Park, S. G. Ji, M. A. Park, J. Y. Kim, *Progress in Photovoltaics: Research and Applications*. **2020**, 28, 1345.

[35] Y. Wang, Y. Yang, C. Zhu, H. Luan, R. Liu, L. Wang, C. Zhao, X. Lv, *ACS Applied Energy Materials*. **2020**, 3, 11177.

[36] W. L. Jeong, K. P. Kim, J. Kim, H. K. Park, J. H. Min, J. S. Lee, S. H. Mun, S. T. Kim, J. H. Jang, W. Jo, D. S. Lee, *Adv Sci (Weinh)*. **2020**, 7, 1903085.

[37] J. Park, H. Yoo, V. Karade, K. S. Gour, E. Choi, M. Kim, X. Hao, S. J. Shin, J. Kim, H. Shim, D. Kim, J. H. Kim, J. Yun, J. h. Kim, *Journal of Materials Chemistry A*. **2020**, 8, 14538.

[38] S. Wang, Z. Jiang, Z. Shen, Y. Sun, H. Guo, L. Wu, J. Zhang, J. Ao, H. Wang, Y. Zhang, *Science China Materials*. **2020**, 64, 288.

[39] S. Ge, H. Xu, Y. Huang, S. K. Karunakaran, R. Hong, J. Li, Y. Mai, E. Gu, X. Lin, G. Yang, *Solar RRL*. **2020**, 4, 2000325.

[40] M. Nakamura, K. Yamaguchi, Y. Kimoto, Y. Yasaki, T. Kato, H. Sugimoto, *IEEE Journal of Photovoltaics*. **2019**, 9, 1863.

[41] T. Gershon, B. Shin, N. Bojarczuk, M. Hopstaken, D. B. Mitzi, S. Guha, *Advanced Energy Materials*. **2015**, 5, 1400849.

[42] G.-X. Liang, Y.-D. Luo, S. Chen, R. Tang, Z.-H. Zheng, X.-J. Li, X.-S. Liu, Y.-

K. Liu, Y.-F. Li, X.-Y. Chen, Z.-H. Su, X.-H. Zhang, H.-L. Ma, P. Fan, *Nano Energy*. **2020**, 73, 104806.

[43] M. Ishaq, H. Deng, S. Yuan, H. Zhang, J. Khan, U. Farooq, H. Song, J. Tang, *Solar RRL*. **2018**, 2, 1800144.

[44] R. Tang, Z.-H. Zheng, Z.-H. Su, X.-J. Li, Y.-D. Wei, X.-H. Zhang, Y.-Q. Fu, J.-T. Luo, P. Fan, G.-X. Liang, *Nano Energy*. **2019**, 64, 103929.

[45] W. Yang, H. S. Duan, B. Bob, H. Zhou, B. Lei, C. H. Chung, S. H. Li, W. W. Hou, Y. Yang, Adv Mater. 2012, 24, 6323.

[46] W. Zhao, G. Wang, Q. Tian, L. Huang, S. Gao, D. Pan, *Solar Energy Materials and Solar Cells*. **2015**, 133, 15.

[47] X. Zhao, X. Chang, D. Kou, W. Zhou, Z. Zhou, Q. Tian, S. Yuan, Y. Qi, S. Wu, *Journal of Energy Chemistry*. **2020**, 50, 9.

[48] Y. Gong, R. Qiu, C. Niu, J. Fu, E. Jedlicka, R. Giridharagopal, Q. Zhu, Y. Zhou, W. Yan, S. Yu, J. Jiang, S. Wu, D. S. Ginger, W. Huang, H. Xin, *Advanced Functional Materials*. **2021**, 31, 2101927.

[49] Y. Qi, Q. Tian, Y. Meng, D. Kou, Z. Zhou, W. Zhou, S. Wu, *ACS Appl Mater Interfaces*. **2017**, 9, 21243.

[50] S. Das, S. K. Chaudhuri, R. N. Bhattacharya, K. C. Mandal, *Applied Physics Letters*. **2014**, 104, 192106.

[51] S. Chen, A. Walsh, X. G. Gong, S. H. Wei, *Adv Mater*. **2013**, 25, 1522.

[52] Y. C. Du, S. S. Wang, Q. W. Tian, Y. C. Zhao, X. H. Chang, H. Q. Xiao, Y. Q. Deng, S. Y. Chen, S. X. Wu, S. Z. Liu, *Advanced Functional Materials*. **2021**,

31, 2010325.

[53] Z.-K. Yuan, S. Chen, H. Xiang, X.-G. Gong, A. Walsh, J.-S. Park, I. Repins, S.-H. Wei, *Advanced Functional Materials*. **2015**, 25, 6733.

[54] Y.-R. Lin, V. Tunuguntla, S.-Y. Wei, W.-C. Chen, D. Wong, C.-H. Lai, L.-K. Liu, L.-C. Chen, K.-H. Chen, *Nano Energy*. **2015**, 16, 438.

[55] H. Hempel, R. Eichberger, I. Repins, T. Unold, *Thin Solid Films*. **2018**, 666, 40.

The table of contents entry:

Anhydrous $SnCl_4$ is substituted with $SnCl_4 \cdot 5H_2O$ to prepare Sn^{4+} precursor solution in air and two solutions containing Sn^{4+} and Sn^{2+} are mixed as the final precursor solution, rendering a feasible scheme to obtain denser films and avoid film cracking. when the ratio of Sn^{4+} to Sn^{2+} is 1:1, the best efficiency of 11.1% for CZTSSe solar cells is obtained.

Guang-Xing Liang[1], Zi-Xuan Yu[1], Zhi-Gao Xie[1], Yang He[1], Jin-Hong Lin[1], Shuo Chen[1], Zhuang-Hao Zheng[1], Jing-Ting Luo[1], Ping Fan[1], Zheng-Hua Su[*1], Hong-Li Ma[2], Xiang-Hua Zhang[2]

Optimizing the ratio of Sn^{4+} and Sn^{2+} in $Cu_2ZnSn(S,Se)_4$ precursor solution via air environment for highly efficient solar cells

ToC figure:

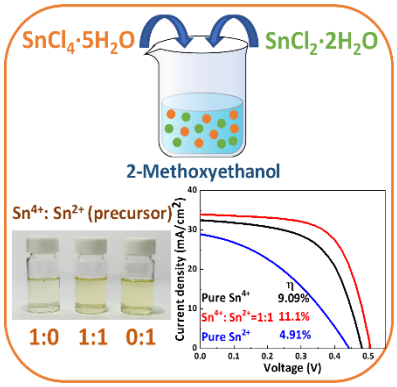

Supporting Information

Optimizing the ratio of Sn^{4+} and Sn^{2+} in $Cu_2ZnSn(S,Se)_4$ precursor solution via air environment for highly efficient solar cells

Guang-Xing Liang[1], *Zi-Xuan Yu*[1], *Zhi-Gao Xie*[1], *Yang He*[1], *Jin-Hong Lin*[1], *Shuo Chen*[1], *Zhuang-Hao Zheng*[1], *Jing-Ting Luo*[1], *Ping Fan*[1], *Zheng-Hua Su*[*1], *Hong-Li Ma*[2], *Xiang-Hua Zhang*[2]

[1]Shenzhen Key Laboratory of Advanced Thin Films and Applications, Key Laboratory of Optoelectronic Devices and Systems, College of Physics and Optoelectronic Engineering, Shenzhen University, Shenzhen, 518060, P. R. China

[2] Univ Rennes, CNRS, ISCR (Institut des Sciences Chimiques de Rennes) UMR 6226, Rennes, F-35000, France

E-mail: zhsu@szu.edu.cn

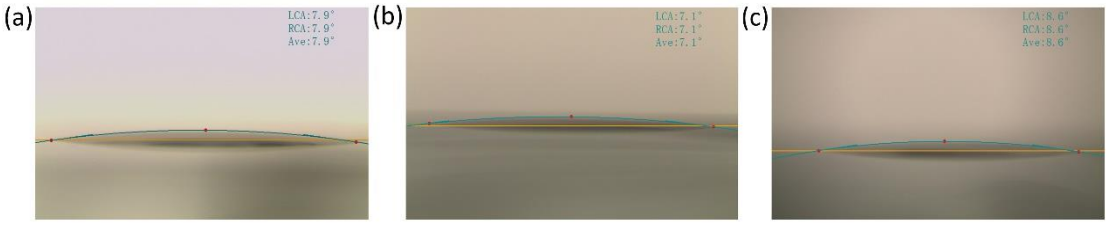

Figure S1. Contact angles of the precursor solutions with 1:0, 1:1, and 0:1 of Sn^{4+} to Sn^{2+} on the Mo substrate, corresponding to (a), (b) and (c), respectively.